Geometrically-driven underground camera modeling and calibration with coplanarity constraints for Boom-type roadheader

***Abstract*—The conventional calibration methods based on perspective camera model are not suitable for underground cameras with two-layer glasses, which are specially designed for explosion-proof and dust removal in coal mine. Underground camera modeling and calibration algorithms are urgently needed to improve the precision and reliability of underground visual measurement systems. This paper presents a novel geometrically-driven underground camera calibration algorithm for a boom-type roadheader. The underground camera model is established under coplanarity constraints, by considering explicitly the impact of refraction triggered by the two-layer glasses and deriving the geometrical relationship of equivalent collinearity equations. On this basis, we perform parameters calibration based on a geometrically-driven calibration model, which is a 2D-2D correspondences between the image points and object coordinates of the plannar target. A hybrid LM–PSO algorithm is further proposed in terms of the dynamic combination of the Levenberg–Marqurdt (LM) and Particle Swarm Optimization (PSO), which optimize the underground camera calibration results by minimizing the error of the nonlinear underground camera model. The experiment results demonstrate that the pose errors caused by the two-layer glass refraction are well corrected by the proposed method. The accuracy of the cutting-head pose estimation has increased by 55.73%, meeting the requirements of underground excavations.**

***Index Terms*—vision-based pose estimation, underground camera model, camera calibration, two-layer glasses, nonlinear optimization**

I. Introduction

VISION-based pose estimation provides an efficient means to get the accurate equipment pose [1, 2, 3], which is also the core technology to realize automatic mining. The vision-based pose estimation system is affected by the harsh environment in the coal mine, such as complex background, dust, water mist, stray lights and so on. Therefore, on account of explosion-proof and dust removal, an underground camera was specially designed with two-layer glasses, such a vision-based underground imaging system extends a combination unit of both the camera and the two-layer glasses. Calibrating such a visual measurement system with two-layer glasses of unknown alignments remains a challenging problem.

The underground imaging system observe a target object through multiple refractive planes is with a non-single viewpoint (non-SVP) [4].The camera calibration methods [5, 6, 7] based on the well-known perspective camera model [8] are not suitable for such a non-SVP imaging system. There is a growing attention on non-SVP systems in underwater environments recently [9, 10, 11, 12]. In the early works of underwater computer vision, the refraction effect are approximated using focal length or lens distortions [13, 14, 15]. However, the approximation approaches usually result in errors in the calibration results due to the non-linear refraction distortion are highly related to the scene geometry. Kwon and Casebolt [16] concluded that a physics-based calibration approach is needed for 3D reconstruction. It is also demonstrated by Treibitz et al. [17] that a single viewpoint (SVP) model is invalid in underwater camera calibration. Physics-based models that account for the refraction effect has attracted researchers' attention. Maas [18] considered a fast and versatile algorithm for the three flat refraction geometric modelling assuming that the image plane is parallel to the refractive interfaces, and the geometric effects are solved iteratively. Treibitz et al. [17] considered a parameterized model with the distance of the lens from the interface, they perform calibration using known target depth and the image plane must be parallel to the interface in their setup as well. Y. J. Chang et al. proposed a multi-view 3D underwater calibration method by modeling the refractive effect using the known scene depth. [19]. The major limitation for the techniques in [17, 18, 19] is that they either assume the image plane parallel to the interface in their setup or need the known target depth. Hence, these technique are not practical for the underground camera refraction calibration in coal mine since we cannot assume the image plane and interface to be parallel and also the target pose is unknown during tunneling. Some stereo underwater calibration methods do not need to know the target pose but require multi-view images. The underwater camera modelling and calibration methods in [20, 21] were developed for a camera with a single-layer waterproof housing device, the scale constraint in the fixed stereo rig makes it affordable to calibrate with unknown target pose. The method requires an approximation estimation of orientation parameters, and the calibration requires to be computed iteratively. [22] presents a calibration model with explicit incorporation of refraction. However it requires a good initial estimation for the interface parameters. The calibration method in [23] for the underwater stereo camera system can obtain a good initial estimation by solving a set of linear equations and refining it by sparse bundle adjustment. The major limit of the above stereo calibration methods in [20, 21, 22, 23] is that the calibration require stereo correspondences, which is not feasible for the single image refraction calibration in the single underground camera setup system. Agrawal et al. [4] proposed a unified theory for flat refractive geometry, and a calibration method was developed on the basis of the axis estimation method. The calibration method in [4] is similar to [24] and was mapped to the classical essential matrix computation and 5-point algorithm [25]. It performs calibration by using a single image with no known target pose and without the assumption that the image

plane is parallel to the interface. However, the major limit of this method is that the coplanarity constraint in the model will be invalid when the rays have a small angle with axis. The angle will become very small when the center axis of the target nearly parallel to the optical axis of the camera during each cutting period, which make it unreliable for this method to be deployed for underground camera refraction calibration in coal mine.

Hence, there are certain requirements that in most existing calibration methods that make them impractical for application in coal mine, the underground camera modeling and calibration methods are urgently needed. This paper proposes a geometrically-driven underground camera modeling and calibration method. The main contributions of this paper are summarized as follows: 1) An underground camera model was established under coplanarity constraints, which considered explicitly the refraction effect triggered by the two-layer glasses and gave the equivalent collinearity equations. 2) A geometrically-driven underground camera calibration model was proposed, which gives 2D-2D correspondences between the image points and object coordinates of the plannar target. 3) A hybrid LM–PSO algorithm is further proposed to optimize the initial underground camera calibration results by minimizing the error of the nonlinear underground camera model. 4) Experiment were designed to validate the proposed calibration algorithm.

The rest of paper is organized as follows: Section II introduces the working principle of vision-based pose estimation system for Boom-type roadheader. Section III puts forward an underground camera model under coplanarity constraints. Section IV presents a geometrically-driven calibration algorithm for underground camera. Section V presents the experimental results. Finally, the full text is summarized and discussed in Section VI.

II. Vision-based Pose Estimation System for Boom-type Roadheader

It is high dust and low illumination in underground roadway tunneling as shown in Fig.1a. In accordance with the planned trajectory, the Boom-type roadheader cuts the coal wall using cutting-head to form the new tunneling face as illustrated in Fig.1b. 16 infrared LEDs assembled in a target are adopted as feature markers to tackle the low illumination, dense-dust and complicated background. A vision-based method is used to measure the cutting-head pose, and the underground camera is mounted on the body of Boom-type roadheader, which collects the image of the infrared LEDs-based target mounted on the cutting arm. Fig.1c shows there are seven coordinate systems in the vision-based cutting-head pose estimation system, including the body coordinate system $O_0X_0Y_0Z_0$, the rotary joints coordinate system $O_1X_1Y_1Z_1$, the lift joints coordinate system $O_2X_2Y_2Z_2$, the expansion joints coordinate system $O_3X_3Y_3Z_3$, the cutting-head coordinate $O_4X_4Y_4Z_4$, the camera coordinate system $O_cX_cY_cZ_c$, and the target coordinate system $O_bX_bY_bZ_b$. Vision-based cutting-head pose estimation can be performed with

$$\mathbf{M}_0^4 = \mathbf{M}_0^c \mathbf{M}_c^b \mathbf{M}_b^4 \tag{1}$$

where $\mathbf{M}_0^c$ denotes the transformation matrix between the body and camera coordinate system, $\mathbf{M}_b^4$ shows the transformation matrix between the target and cutting-head coordinate system, $\mathbf{M}_c^b$ expresses the transformation matrix between the camera and target coordinate system, $\mathbf{M}_0^4$ denotes the transformation matrix between the body and cutting-head coordinate system.

The rigid transformation matrix of $\mathbf{M}_0^c$ and $\mathbf{M}_b^4$ need to be pre-calibrated. While $\mathbf{M}_c^b$ can be acquired by the proposed geometrically-driven underground camera modeling and calibration algorithm, which is described in Section III, IV.

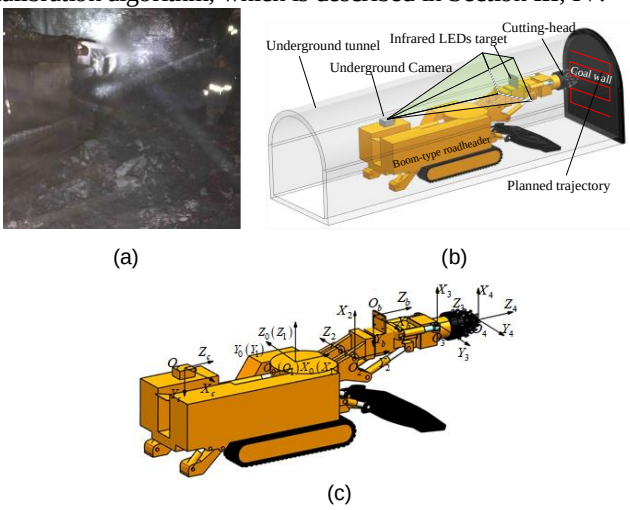

Fig. 1. Boom-type roadheader and its visual system. (a) Tunneling environment of Boom-type roadheader (b) Schematic of vision-based pose estimation. (c) The coordinate systems of Boom-type roadheader.

The cutting-head pose estimation is based on the underground camera modeling and calibration. The geometric model of the underground camera considered explicitly the refraction effect of the two-layer glasses, and established modified collinearity equation. On this basis, we build a 2D-2D correspondences between the image points and the object coordinates of the target, and the pose estimation error caused by refraction effect can be compensated. The main modules of the proposed methods are described in Fig.2.

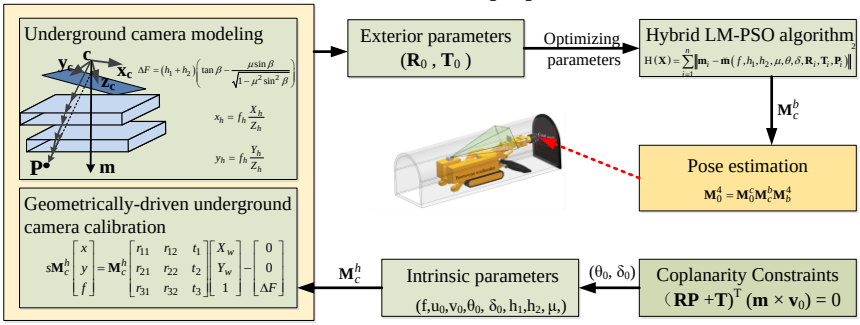

Fig. 2. Outline of the geometrically-driven pose estimation methods.

III. Underground Camera Modeling

A. Underground Camera structure

The underground camera is a specially designed hollow cylindrical structure with two-layer glasses for explosion- proof and dust removal as shown in Fig.3.

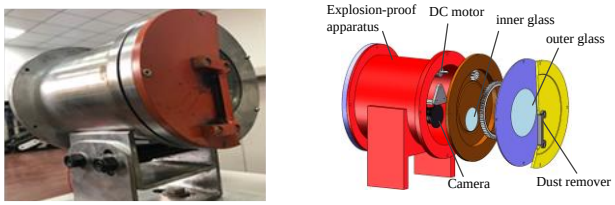

Fig. 3. Underground camera and its internal structure.

The inner-layer explosion-proof glass was mounted on the inner flange plate. The outer-layer glass was mounted on the outer flange as the hub part of the big gear, which was coaxial to the hollow cylindrical structure. A DC motor was mounted in the front of the cylindrical structure, and the output shaft of the motor passes through the inner flange and connects to a pinion. The big gear engages with the pinion and drive the outer-layer glass to rotate. Hence, the fan-shaped dust remover mechanism can clear away the water mist and dust using the stationary brush.

B. Modeling

The imaging system of underground camera extends a combination unit which consists of the camera and the two-layer glasses, and collinearity does not prevail in this non-single viewpoint system. Hence, an underground camera model based on the equivalent collinearity equation in the virtual imaging system is proposed. The virtual imaging system is illustrated in Fig. 4a and 4b, which take **c'** as the virtual perspective center, the outer-layer glass interface as the virtual image plane, and F-ΔF as the virtual focal length along the virtual axis **m**. The virtual axis **m** is the normal to the two-layer glasses and passing through the camera perspective center.

The underground camera model is described with the following parameters: β, the incidence angle; α, the refraction angle; *f*, the actual focal length from the actual perspective center **c** to the image plane; F, the distance from the actual perspective center **c** to the outer-layer glass interface; ΔF, the offset from actual perspective center **c** to virtual perspective center **c'**; d, the camera incoming ray offset on the two-layer glasses interface; h_1, the thickness of the outer-layer glass; h_2, the thickness of the inner-layer glass; n_{air}, the refractive index of air; n_{glass}, the refractive index of glass.

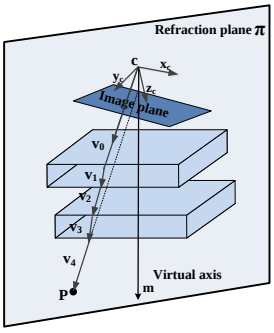

(a)

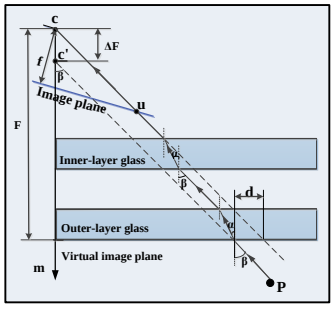

(b)

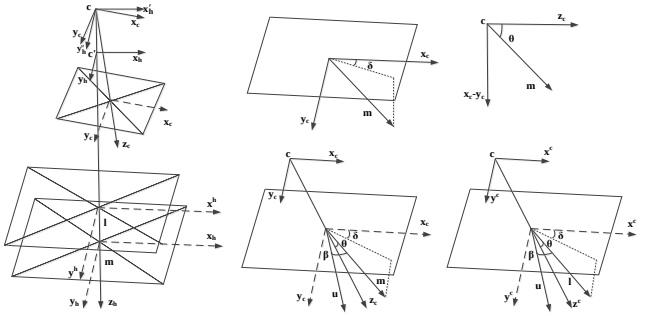

(c)

Fig. 4. (a) The entire light-path lies on the same plane of **π**. (b) The incoming ray in turn refracted at the two-layer glasses interface, and then pass through the camera perspective center. (c) The diagram of the mounting angle offset in the underground camera imaging system. The normal of **l** to the inner glass is parallel to the normal of **m** to the outer glass.

The two-layer glasses on the underground camera can be guaranteed to be parallel with relatively high precision by machining and assembly precision. However, the camera optical axis is not guaranteed to be orthogonal to the double layers of glass in general situation, i.e., there is a mounting angle offset between the camera image plane and the glass interface plane. The transformation relation between the camera coordinate system and the virtual imaging system is illustrated in Fig. 4c. The camera coordinate system is represented by $\mathbf{c}x_c y_c z_c$ and the virtual imaging system is represented by $\mathbf{c'}x_h y_h z_h$. The angle between the camera's optical axis $\mathbf{z_c}$ and the virtual axis **m** is defined as θ, and the projection vector of the virtual axis **m** on the image plane x_c-y_c with respect to the camera's x-axis is defined as δ. The rotation matrix $\mathbf{M}_c^h$ between the camera coordinate system and the virtual imaging system can be expressed as

$$\mathbf{M}_c^h = \begin{bmatrix} \sin^2\delta(1-\cos\theta)+\cos\theta & -\sin\delta\cos\delta(1-\cos\theta) & -\sin\theta\cos\delta \\ -\sin\delta\cos\delta(1-\cos\theta) & \cos^2\delta(1-\cos\theta)+\cos\theta & -\sin\theta\sin\delta \\ \sin\theta\cos\delta & \sin\theta\sin\delta & \cos\theta \end{bmatrix} \tag{2}$$

The third row of $\mathbf{M}_c^h$ denotes the virtual axis vector **m** in the camera coordinate system,

$$\mathbf{m} = [\sin\theta\cos\delta, \sin\theta\sin\delta, \cos\theta] \tag{3}$$

The incidence angle β can be obtained from the image coordinate **u** and the vector **m** using the following equation

$$\cos\beta = \frac{(\mathbf{m})^{\mathrm{T}}\mathbf{u}}{\|\mathbf{u}\|} \tag{4}$$

The refraction angle α is calculated by $\mu = \sin\alpha / \sin\beta$, where μ denotes the relative refractive index of the air and glass.

The incoming ray offset *d* is calculated by

$$d = h_1(\tan\beta - \tan\alpha) + h_2(\tan\beta - \tan\alpha) \tag{5}$$

where h_1 represents the thickness of the outer-layer glass, and h_2 represents the thickness of the inner-layer glass.

The offset ΔF from actual perspective center c to virtual perspective center **c'** can be expressed as

$$\Delta F = d / \tan\beta = (h_1 + h_2)\left(\tan\beta - \frac{\mu\sin\beta}{\sqrt{1-\mu^2\sin^2\beta}}\right) \tag{6}$$

Assuming $\mathbf{P}_c=[X_c, Y_c, Z_c]^T$ is a 3D spatial point in the camera coordinate system. By combing with (2), the $\mathbf{P}_c$ in the virtual imaging system can be expressed as

$$\mathbf{P}_h = \mathbf{M}_c^h \mathbf{P}_c - \mathbf{T}_c^h = [X_h, Y_h, Z_h]^T \tag{7}$$

where $\mathbf{T}_c^h = [0, 0, \Delta F]^T$ is the translation vector $\mathbf{T}_c^h$ between the camera coordinate system and the virtual imaging system.

Similarly, assume that $\mathbf{u} = [x, y, f]^T$ is the image coordinate of $\mathbf{P}_c$ in the camera coordinate system. An auxiliary coordinate system of $\mathbf{cx'_h y'_h z'_h}$ is set up as shown in Fig. 4c, which take the actual perspective center c as the origin, the axis $\mathbf{x'_h}$, $\mathbf{y'_h}$, $\mathbf{z'_h}$ are parallel to the axis $\mathbf{x_h}$, $\mathbf{y_h}$, $\mathbf{z_h}$ in the virtual imaging system of $\mathbf{c'x_h y_h z_h}$, respectively. The image point $\mathbf{u}$ in the auxiliary coordinate system can be expressed as

$$\mathbf{u}'_h = \mathbf{M}_c^h \mathbf{u} = [x_h, y_h, f_h]^T \tag{8}$$

According to the geometrical relation that the 3D-vector $\mathbf{u}'_h$ is parallel to the 3D-vector $\mathbf{P}_h$, and they can form the same plane when $\mathbf{u}'_h$ and $\mathbf{P}_h$ intersect with the virtual axis $\mathbf{m}$, respectively. Therefore, the modified collinearity equation in the virtual imaging system can be defined as

$$x_h = f_h \frac{X_h}{Z_h}, \; y_h = f_h \frac{Y_h}{Z_h} \tag{9}$$

The collinearity equation forms the geometric model of underground camera based on equivalent focal length in the virtual imaging system, which considered explicitly the impact of refraction triggered by the two-layer glasses and preserve the collinearity relation. Notice that the additional parameters θ, δ, h_1, h_2 and μ are introduced in the underground camera model.

IV. Geometrically-driven Underground Camera Calibration

A. Axis Estimation with Coplanarity Constraints

As illustrated in Fig. 4a, $\mathbf{P}=[X_w, Y_w, Z_w]^T$ is a 3D spatial point in the object coordinate system, the direction vectors of each segment of the light-path are $\mathbf{v}_0$, $\mathbf{v}_1$, $\mathbf{v}_2$, $\mathbf{v}_3$, $\mathbf{v}_4$, respectively. According to Snell's law, the incident ray, the refracted ray and the normal lie on the same plane. Considering the two-layer glasses are parallel, the entire light-path is coplanar and lies on the refraction plane $\boldsymbol{\pi}$ when the light rays pass through the two-layer glasses. The virtual axis $\mathbf{m}$ and the entire light-path are on the same plane of $\boldsymbol{\pi}$, and the last refracted ray $\mathbf{v}_0$ intersect with the axis $\mathbf{m}$. Let $\mathbf{R}$ and $\mathbf{T}$ be the rotation and translation matrix between the object and camera coordinates system, $\mathbf{P}_c=\mathbf{RP}+\mathbf{T}$ is the 3D point in the camera coordinate system and it is also lie on $\boldsymbol{\pi}$. According to [4], the coplanarity constraint for each 3D point can be defined as

$$(\mathbf{RP}+\mathbf{T})^T (\mathbf{m} \times \mathbf{v}_0) = 0 \tag{10}$$

where $(\mathbf{m}\times\mathbf{v}_0)$ is the normal of the plane $\boldsymbol{\pi}$.

The coplanarity constraint can be further expanded as the following linear equation system

$$\underbrace{\begin{bmatrix} (\mathbf{P}(1)^T \otimes \mathbf{v}_0(1)^T) & \mathbf{v}_0(1)^T \\ \vdots & \vdots \\ (\mathbf{P}(N)^T \otimes \mathbf{v}_0(N)^T) & \mathbf{v}_0(N)^T \end{bmatrix}}_{\mathbf{B}} \begin{bmatrix} \mathbf{E}(:) \\ \mathbf{s} \end{bmatrix} = 0 \tag{11}$$

where N (N>=11) points are taken to form a N×12 matrix of $\mathbf{B}$. $\mathbf{v}_0(i)$ represent the direction vector of the last refracted ray corresponding to each 3D point $\mathbf{P}(i)$. $\mathbf{E}(:)$ denotes the column vectors of the matrix $\mathbf{E}$. $\mathbf{E}=[\mathbf{m}]_\times\mathbf{R}$, $[\mathbf{m}]_\times$ denotes the 3×3 skew-symmetric matrix of the vector $\mathbf{m}$; $\mathbf{s}=\mathbf{m}\times\mathbf{T}$, × denotes the cross-product. ⊗ represents the kronecker product.

Therefore, $\mathbf{E}$ and $\mathbf{s}$ can be obtained by the right null singular vector of $\mathbf{B}$. In addition, 11-point linear algorithm or 8-point algorithm can also be used to obtain $\mathbf{E}$ and $\mathbf{s}$ [4, 8, 18]. Since $\mathbf{m}^T\mathbf{E}= \mathbf{m}^T[\mathbf{m}]_\times\mathbf{R} =0$, the axis $\mathbf{m}$ can be calculated as the left null singular vector of $\mathbf{E}$.

B. Calibration of Underground Camera Parameters

The calibration process is divided into two steps. First, without the two-layer glasses, the camera's standard intrinsic parameters are acquired can be obtained by the calibration technique proposed by Zhang [6] or Steger [7], including the principal point (u_0, v_0) and focal length f, and the radial and tangential distortion parameters k_1, k_2, p_1, and p_2. Then, with the two-layer glasses, the proposed geometrically-driven calibration algorithm is performed, which involves the additional underground camera intrinsic parameters of θ, δ, h_1, h_2, μ and extrinsic parameters of $\mathbf{R}$ and $\mathbf{T}$.

The parameters h_1, h_2 and μ are assumed to be the known constants here. On the basis of the results of axis estimation in Section IV.A and the definition of virtual axis $\mathbf{m}$ in (3), let $\mathbf{m}=[m_1,m_2,m_3]$, the parameters of θ and δ can be solved with the following equation

$$\theta = \arccos(m_3), \; \delta = \arctan(m_2 / m_1) \tag{12}$$

In accordance with the modified collinearity equation (9), the relationship between a 3D spatial point in the object coordinate system and its image projection can be expressed by the following matrix equation.

$$s\mathbf{M}_c^h \begin{bmatrix} x \\ y \\ f \end{bmatrix} = \mathbf{M}_c^h \begin{bmatrix} r_{11} & r_{12} & r_{13} & t_1 \\ r_{21} & r_{22} & r_{23} & t_2 \\ r_{31} & r_{32} & r_{33} & t_3 \end{bmatrix} \begin{bmatrix} X_w \\ Y_w \\ Z_w \\ 1 \end{bmatrix} - \begin{bmatrix} 0 \\ 0 \\ \Delta F \end{bmatrix} \tag{13}$$

$$[\mathbf{R} \quad \mathbf{T}] = \begin{bmatrix} r_{11} & r_{12} & r_{13} & t_1 \\ r_{21} & r_{22} & r_{23} & t_2 \\ r_{31} & r_{32} & r_{33} & t_3 \end{bmatrix}, \; \mathbf{M}_c^h = \begin{bmatrix} M_{11} & M_{12} & M_{13} \\ M_{21} & M_{22} & M_{23} \\ M_{31} & M_{32} & M_{33} \end{bmatrix}$$

where, s is an arbitrary scale factor. The perspective center offset ΔF can be obtained by (6). The rotation matrix between the camera coordinate system and virtual imaging system $\mathbf{M}_c^h$ can be acquired by (2) with the θ and δ.

Since Z_w is equal to 0 when the calibration is carried out with the single planar target, (13) can be simplified with

$$s\mathbf{M}_c^h \begin{bmatrix} x \\ y \\ f \end{bmatrix} = \mathbf{M}_c^h \begin{bmatrix} r_{11} & r_{12} & t_1 \\ r_{21} & r_{22} & t_2 \\ r_{31} & r_{32} & t_3 \end{bmatrix} \begin{bmatrix} X_w \\ Y_w \\ 1 \end{bmatrix} - \begin{bmatrix} 0 \\ 0 \\ \Delta F \end{bmatrix} \tag{14}$$

Let $\mathbf{X} = [r_{11}, r_{12}, r_{21}, r_{22}, r_{31}, r_{32}, t_1, t_2, t_3]^T$, (14) can be rewritten as the following equation system

$$\begin{bmatrix} A_{11} & A_{12} & A_{13} & A_{14} & A_{15} & A_{16} & A_{17} & A_{18} & A_{19} \\ A_{21} & A_{22} & A_{23} & A_{24} & A_{25} & A_{26} & A_{27} & A_{28} & A_{29} \end{bmatrix} \mathbf{X} = \begin{bmatrix} x_h \Delta F \\ y_h \Delta F \end{bmatrix} \tag{15}$$

where,

$$A_{11}= x_h M_{31} X_w - f_h M_{11} X_w,\ A_{12}= x_h M_{31} Y_w - f_h M_{11} Y_w,$$
$$A_{13}= x_h M_{32} X_w - f_h M_{12} X_w,\ A_{14}= x_h M_{32} Y_w - f_h M_{12} Y_w,$$
$$A_{15}= x_h M_{33} X_w - f_h M_{13} X_w,\ A_{16}= x_h M_{33} Y_w - f_h M_{13} Y_w$$
$$A_{17}= x_h M_{31} - f_h M_{11},\ A_{18}= x_h M_{32} - f_h M_{12},$$
$$A_{19}= x_h M_{33} - f_h M_{13}$$
$$A_{21}= y_h M_{31} X_w - f_h M_{21} X_w,\ A_{22}= y_h M_{31} Y_w - f_h M_{21} Y_w,$$
$$A_{23}= y_h M_{32} X_w - f_h M_{22} X_w,\ A_{24}= y_h M_{32} Y_w - f_h M_{22} Y_w,$$
$$A_{25}= y_h M_{33} X_w - f_h M_{23} X_w,\ A_{26}= y_h M_{33} Y_w - f_h M_{23} Y_w$$
$$A_{27}= y_h M_{31} - f_h M_{21},\ A_{28}= y_h M_{32} - f_h M_{22},$$
$$A_{29}= y_h M_{33} - f_h M_{23}$$

Stacking equations for 2N correspondences when N points are taken to (15), it can be written in matrix equation as **LX** = **b**. The extrinsic parameters of **R** and **T** can be recovered by

$$\mathbf{X} = (\mathbf{L}^{\mathrm{T}}\mathbf{L})^{-1}\mathbf{L}^{\mathrm{T}}\mathbf{b},$$
$$\mathbf{r}_3 = \mathbf{r}_1 \times \mathbf{r}_2$$

where **L** is a 2N×9 matrix, and $\mathbf{r}_i$ denotes the i[th] column of the rotation matrix $\mathbf{R}=[\mathbf{r}_1,\mathbf{r}_2,\mathbf{r}_3]$.

In accordance with the geometrically-driven extrinsic parameters calibration equation (15), a 2D-2D correspondences between the image points and object coordinates of the plannar target are established. The underground camera parameters are obtained in the case that the camera is internally calibrated and with known refractive index as well as the thickness of glasses. Notice that we do not assume that image plane is parallel to the apparatus interface and we do not request explicit knowledge of object point coordinates.

C. Nonlinear Optimization of Underground Camera Parameters

The underground camera modeling and calibration algorithm in Section III and IV.B can used to obtain a good initial solution of underground camera parameters. In this section, a hybrid LM–PSO algorithm is proposed to further perform nonlinear optimization of the initial underground camera calibration results because of the easy and quick convergence the LM [25,26,27]and the global optimization ability of the PSO [28,29]. Given there are *n* points on the image plane, the hybrid LM-PSO algorithm can be performed with

Find: $\mathbf{X} = [\theta, \delta, \alpha, \beta, \gamma, t_x, t_y, t_z]$

Min: $\mathrm{H}(\mathbf{X}) = \sum_{i=1}^{n} \left\| \mathbf{U}_i - \breve{\mathbf{U}}(f, h_1, h_2, \mu, \theta, \delta, \mathbf{R}_i, \mathbf{T}_i, \mathbf{P}_i) \right\|^2$

Among which, $\mathbf{U}_i=((u_i-u_0)d_x, (v_i-v_0)d_y)$ is the measured value of image coordinates, $\breve{\mathbf{U}}(f, h_1, h_2, \mu, \theta, \delta, \mathbf{R}_i, \mathbf{T}_i, \mathbf{P}_i)$ is the projection point of 3D point $\mathbf{P}_i$ in image plane according to (14), H(**X**) is the object function that needs to be minimized, which is a nonlinear minimization problem. **X** is the optimal solution once H(**X**) find minimum error. The image pixel deviation between the measured and projected values can be expressed with the following equations

$$F_{ix}(\mathbf{X}) = (u_i - u_0)d_x - \breve{\mathbf{U}}_x(f, h_1, h_2, \mu, \theta, \delta, \mathbf{R}_i, \mathbf{T}_i, \mathbf{P}_i)$$
$$F_{iy}(\mathbf{X}) = (v_i - v_0)d_y - \breve{\mathbf{U}}_y(f, h_1, h_2, \mu, \theta, \delta, \mathbf{R}_i, \mathbf{T}_i, \mathbf{P}_i)$$

where $\breve{\mathbf{U}}_x(f, h_1, h_2, \mu, \theta, \delta, \mathbf{R}_i, \mathbf{T}_i, \mathbf{P}_i)$ is the x-axis projection of image plane, $\breve{\mathbf{U}}_y(f, h_1, h_2, \mu, \theta, \delta, \mathbf{R}_i, \mathbf{T}_i, \mathbf{P}_i)$ is the y-axis projection of image plane. The focal length *f*, principle points (u_0, v_0), and pixel size (d_x, d_y) are standard camera intrinsic parameters, the thickness of the outer glass h_1, the thickness of the inner glass h_2, and the relative refractive index μ are the additional underground camera intrinsic parameters. $\mathbf{R}_i(\alpha, \beta, \gamma)$ and $\mathbf{T}_i(t_x, t_y, t_z)$ are the rotation and translation matrix, respectively. (α, β, γ) are the Euler angles of the rotation matrix $\mathbf{R}_i$.

According the initial solution $\mathbf{X}_l^0$ of underground camera parameters, the constraint conditions of the population particle's position $\mathbf{X}_l$ and velocity $\mathbf{V}_l$ were respectively set as

$$(1-h_l)\mathbf{X}_l^0 \le \mathbf{X}_l \le (1+h_l)\mathbf{X}_l^0$$
$$\mathbf{X}_{l\min=}(1-h_l)\mathbf{X}_l^0,\quad \mathbf{X}_{l\max=}(1+h_l)\mathbf{X}_l^0$$
$$(1-h_l)\mathbf{X}_l^0/2 \le \mathbf{V}_l \le (1+h_l)\mathbf{X}_l^0/2$$
$$\mathbf{V}_{l\min=}(1-h_l)\mathbf{X}_l^0/2,\quad \mathbf{V}_{l\max=}(1+h_l)\mathbf{X}_l^0/2 \qquad (16)$$

where the dimension of particle is 8, $X_1=\theta$, $X_2=\delta$, $X_3=\alpha$, $X_4=\beta$, $X_5=\gamma$, $X_6= t_x$, $X_7= t_y$, $X_8=t_z$. h_l is the step length of X_l. l=1,…,8.

Firstly, PSO is called to generate the $\mathbf{V}_{jl}^0$ and $\mathbf{X}_{jl}^1$

$$\mathbf{V}_{jl}^0 = rand(N,1)(\mathbf{V}_{l\max} - \mathbf{V}_{l\min}) + \mathbf{V}_{l\min}$$
$$\mathbf{X}_{jl}^1 = \mathbf{X}_{jl}^0 + \mathbf{V}_{jl}^0,\ \mathbf{X}_{jl}^0 = \mathbf{X}_l^0 \qquad (17)$$

where, *N* is the population size of PSO, *N*=20, *j*=1,…,*N*. *rand*(*N*, 1) is a random number between [0, 1].

Let the position of *p*th generation be represented by $\mathbf{X}_{jl}^p = (X_{j1}^p, X_{j2}^p, \ldots, X_{j8}^p)^{\mathrm{T}}$, its speed is represented as $\mathbf{V}_{jl}^p = (V_{j1}^p, V_{j2}^p, \ldots, V_{j8}^p)^{\mathrm{T}}$. The renewal equations of speed and position are expressed as

$$\mathbf{V}_{jl}^{p+1} = w\mathbf{V}_{jl}^p + c_1 rand(N,1)\left(pbest - \mathbf{X}_{jl}^p\right) + c_2 rand(N,l)\left(gbest - \mathbf{X}_{jl}^p\right)$$
$$\mathbf{X}_{jl}^{p+1} = \mathbf{X}_{jl}^p + \mathbf{V}_{jl}^{p+1} \qquad (18)$$

where *w* is the inertia weight, c_1 and c_2 are the learning factor, here $c_1=c_2=1.5$. *pbest* and *gbest* are respectively the position of the personal best particle and the global best particle. *pbest* and *gbest* can be obtained by the comparison with fitness value of each particle, the fitness can be calculated with the objective function $\mathrm{H}\left(\mathbf{X}_j^p\right)$. The inertia weight dynamically changed with

$$w = w_{\max} - (w_{\max} - w_{\min}) \cdot p / G_{\max} \qquad (19)$$

where, the minimum inertia weight $w_{\min}$=0.4, maximum inertia weight $w_{\max}$=0.9, *p* represents the number of iterations.

Then, the LM algorithm was called with four pairs of (u_i, v_i) and $\mathbf{P}_i$, $(i=1,\ldots,4)$ to optimize each global best particle that are generated by PSO process with the following equations

$$\mathbf{X}_{ij}^{k+1,p} = \mathbf{X}_{ij}^{k,p} + \hat{\boldsymbol{\delta}}_{ij}^{k,p}$$
$$\hat{\boldsymbol{\delta}}_{ij}^{k,p} = \left(\mathbf{A}_k^{\mathrm{T}}\mathbf{A}_k + \lambda_k \mathbf{I}\right)^{-1}\mathbf{A}_k^T\mathbf{F}_{ij}^{k,p} \qquad (20)$$

where, $\mathbf{X}_{ij}^{\mathbf{k,p}}$ is the *j*th particle that has been iterated to *k*th by LM and *p*th by PSO. $\hat{\boldsymbol{\delta}}_{ij}^{k,p}$ is the vector deviation, **I** is an eight order unit matrix. λ_k is the weight coefficient. $\mathbf{F}_{ij}^{k,p}$ represents $\mathbf{F}_i\left(\mathbf{X}_j^{k,p}\right)$. $\mathbf{A}_k$ is the first-order partial derivative matrix of $\breve{\mathbf{U}}_{ij}^{k,p}$ with respect to the parameter variables θ, δ, α, β, γ, t_x, t_y and t_z.

$$\mathbf{A}_k = \begin{bmatrix} \frac{\partial \breve{\mathbf{U}}_{1xj}^{k,p}}{\partial \theta_j^{k,p}} & \cdots & \frac{\partial \breve{\mathbf{U}}_{1xj}^{k,p}}{\partial t_{zj}^{k,p}} \\ \vdots & & \vdots \\ \frac{\partial \breve{\mathbf{U}}_{4yj}^{k,p}}{\partial \theta_j^{k,p}} & \cdots & \frac{\partial \breve{\mathbf{U}}_{4yj}^{k,p}}{\partial t_{zj}^{k,p}} \end{bmatrix}, \mathbf{F}_{ij}^{k,p} = \begin{bmatrix} F_{ixj}^{k,p}(\mathbf{X}) \\ F_{iyj}^{k,p}(\mathbf{X}) \end{bmatrix}$$

In addition, boundary conditions are adopted to limit the position or velocity of the particle within the feasible search space. Once iteration accuracy meet the required accuracy ε_0, $H(X_j^{k,p}) \leqslant \varepsilon_0$, that is the global minima has been found in the LM-PSO process, the hybrid LM-PSO algorithm will stop, and generate the globally optimal solution **X**. Otherwise, the particle swarm will be updated again by PSO and optimized by LM algorithm until the iteration accuracy meet the requirements. The final results **X** will be the optimized underground camera parameters. The pose estimation accuracy can be improved by about 6% through non-linear optimization. The total computation time for each calibration is about 0.67s in Microsoft Visual C++ 2010 when using Intel(R) Core™ i5-6200U Processor, and the non-linear optimization time accounts for about 33% of the total time. The non-linear optimization will mainly be used for the underground camera parameters offline calibration, and it will be ignored during the tunneling process.

V. Experimental Results

Underground camera calibration and cutting-head pose estimation platform was setup for Boom-type roadheader as shown in Fig.5. The system mainly includes the Boom-type roadheader EBZ160, infrared LEDs SE3470, Vicon Tracker motion capture system, camera MV_EM130M (Microvision), underground explosion-proof apparatus, 250mm×250mm infrared LED target, checkerboard AFT-MCT-OV430, translation stage, PC computer and so on. The image resolution of the camera is 1280×960 pixels. The calibration platform shown in Fig. 5b,c were with a combination unit of the two-layer glasses and camera, which used to make a comparison and analysis between the non-glass configuration and the two-layer glasses configuration. The refractive index of the explosion-proof glass is 1.539, the thickness of the inner glass and outer glass are respectively 10.01mm and 10.02mm.

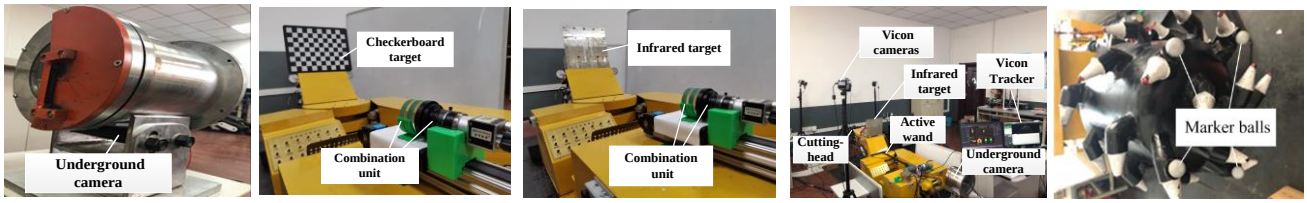

Fig. 5. Underground camera calibration and cutting-head pose estimation system (a) Underground camera. (b) Camera calibration with the checkerboard. (c) Camera calibration with the infrared LEDs target. (d) Cutting-head pose estimation with underground camera. (e) Cutting-head with marker balls of Vicon Tracker system.

The experiment with checkerboard as shown in Fig. 5b was carried out to validate the effectiveness of the proposed algorithm in a controlled indoor environment with a good visibility condition. The distance between the checkerboard and the camera is about 900 mm. The experiment with infrared LEDs target as shown in Fig. 5c was carried out to validate the feasibility of the proposed algorithm in the simulated low illumination underground environment in laboratory. The distance between the target and the camera is about 1500 mm. The checkerboard images and infrared target images from different orientations were collected with and without the two-layer glasses as shown in Fig. 6a,b and Fig.7a,b. The intrinsic camera parameters were calibrated by Zhang's [6]. Intrinsic camera parameters were as follows: f_x=1386 pixel, f_y=1387 pixel, u_0=651.60 pixel, v_0=476.70 pixel, k_1=-0.107, k_2=0.147, p_1=-0.001, p_2=0.000. The lens distortion of the images collected in two-layer glasses configuration were first to be corrected with the above parameters. Then, the additional underground camera intrinsic parameters and the extrinsic parameters were estimated based on the proposed calibration algorithm. Meantime, we computed the reprojection image points with the calibration results according to the proposed underground camera model. The proposed algorithm were made a fully comparison with Agrawal's[4].

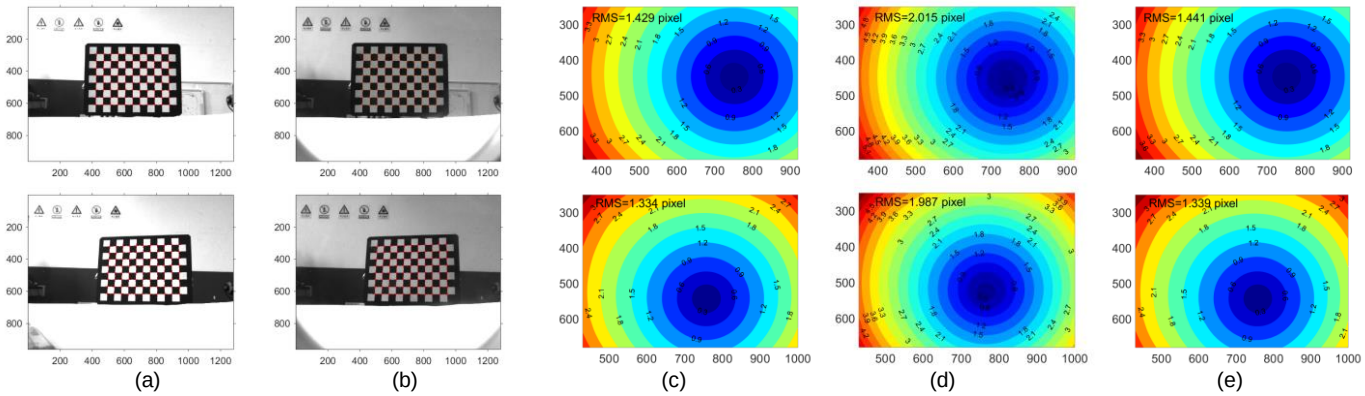

Fig. 6. From left to right were the checkerboard images and corresponding results. (a) Images of the checkerboard target in non-glass configuration, together with the extracted corner (indicated by cross). (b) Images of the checkerboard target in two-layer glasses configuration, together with the extracted corner (indicated by cross) (c) The contour map of the actual image distortion distribution, which describes the image deviation of the extracted corners from Fig.6a to Fig.6b. (d) The contour map of reprojection image distortion distribution by Agrawal's, which describes the image

deviation from the extracted corners in Fig.6a to the reprojection image points by Agrawal's (e) The contour map of reprojection image distortion distribution by ours, which describes the image deviation from the extracted corners in Fig.6a to the reprojection image points by ours.

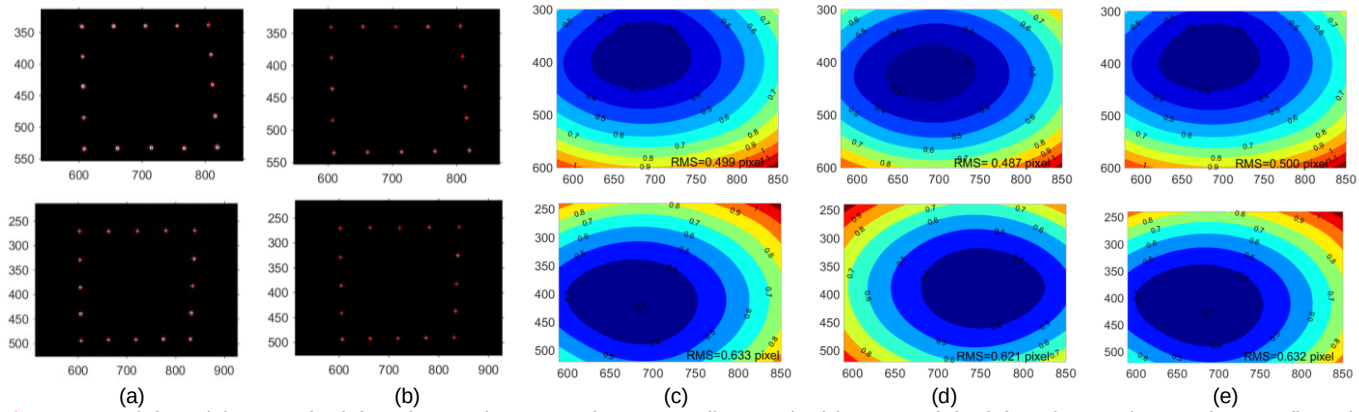

(a) (b) (c) (d) (e)

Fig. 7. From left to right were the infrared target images and corresponding results.(a)Images of the infrared target in non-glass configuration, together with the extracted spot center (indicated by cross).(b)Images of the infrared target in two-layer glasses configuration, together with the extracted spot center (indicated by cross).(c)The contour map of actual image distortion distribution, which describes the image deviation of the extracted spot center from Fig.7a to Fig.7b (d)The contour map of reprojection image distortion distribution by Agrawal's, which describes the image deviation from the extracted spot center in Fig.7a to the reprojection image points by Agrawal's. (e)The contour map of reprojection image distortion distribution by ours, which describes the image deviation from the extracted spot center in Fig.7a to the reprojection image points by ours.

The results shows that the reprojection image distortion distribution in Fig.6d,e and Fig.7d,e were both consistent with the actual image distortion distribution in Fig.6c and Fig.7c, respectively, and the root-mean-square (RMS) errors indicates that reprojection image distortion distribution by ours were closer to the actual distortion distribution in comparison with Agrawal's[4]. Fig.8a,b,c gives the actual and rectified image residuals distribution.

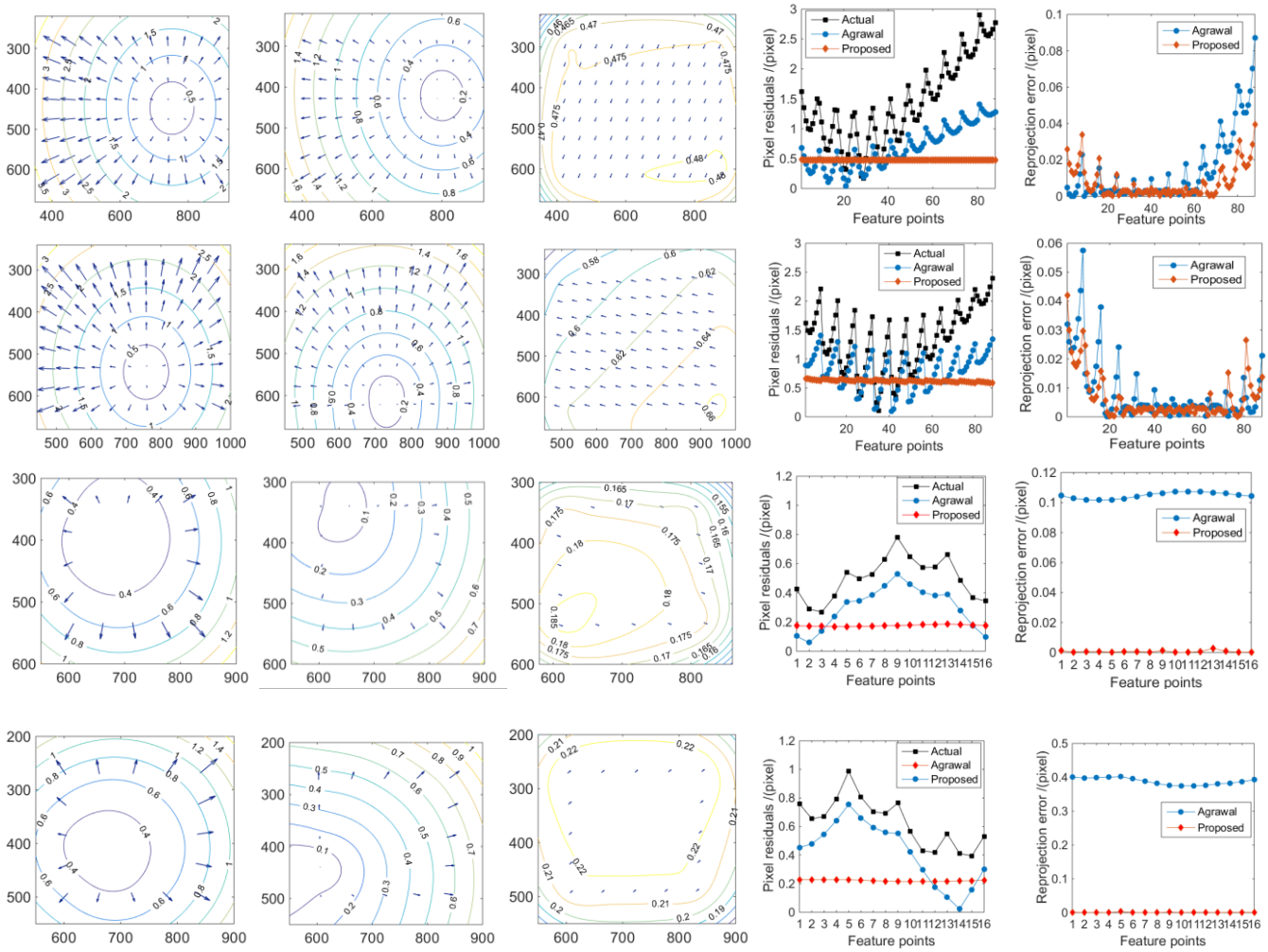

(a) (b) (c) (d) (e)

Fig. 8. The calibration comparison results of detected feature points. From top to bottom were corresponding to the checkerboard images in two orientations and infrared target images in two orientations. (a) The actual image residuals. (b) The rectified image residuals by Agrawal's. (c) The rectified image residuals by proposed algorithm. (d) The comparison of the actual and rectified residuals. (e) The comparison of reprojection errors.

TABLE I
CALIBRATION RESULTS OF CHECKERBOARD FROM TWO ORIENTATIONS

		X/(mm)	Y/(mm)	Z/(mm)	ω/(°)	φ/(°)	κ/(°)
1	GT	150.290	86.686	904.661	6.187	1.107	179.964
	Zhang's	149.780	86.833	897.642	6.188	1.107	179.963
	Agrawal	149.972	86.805	901.688	6.187	1.106	179.964
	Proposed	150.153	86.969	904.682	6.188	1.107	179.964
2	GT	189.617	90.545	890.053	13.648	-8.587	178.393
	Zhang's	189.079	90.205	883.026	13.649	-8.588	178.392
	Agrawal	189.404	90.208	886.379	13.648	-8.589	178.393
	Proposed	189.211	90.444	890.082	13.649	-8.587	178.392

TABLE II
CALIBRATION RESULTS OF INFRARED TARGET FROM TWO ORIENTATIONS

		X/(mm)	Y/(mm)	Z/(mm)	ω/(°)	φ/(°)	κ/(°)
1	GT	70.297	-51.766	1683.500	-18.737	-3.012	-0.800
	Zhang's	70.115	-51.391	1676.538	-18.739	-3.014	-0.801
	Agrawal	70.313	-51.473	1679.889	-18.738	-3.013	-0.800
	Proposed	70.496	-51.685	1683.553	-18.738	-3.012	-0.801
2	GT	74.189	-100.555	1502.470	20.489	-1.375	-0.761
	Zhang's	74.012	-100.184	1495.448	20.489	-1.374	-0.760
	Agrawal	74.319	-100.481	1498.779	20.450	-1.375	-0.760
	Proposed	74.368	-100.713	1502.466	20.488	-1.376	-0.761

Fig. 8d shows that the RMS of the actual image residuals were 1.429, 1.334, 0.499, and 0.633 pixels, respectively; the RMS of the rectified image residuals by ours were 0.477, 0.621, 0.176 and 0.221 pixels; the RMS of the rectified image residuals by Agrawal's were 0.680, 0.797, 0.298 and 0.420 pixels. The results demonstrated that the proposed algorithm can achieve better rectified effect in comparison with Agrawal's. Fig. 8e further shows that the reprojection error using ours were less than Agrawal's, it verified that proposed model can better represent the two-layer glasses refraction than Agrawal's. To assess the pose calibration accuracy by the proposed calibration algorithm, the calibration results were given comparison with Zhang's, Agrawal's and the ground-truth (GT). The collected checkerboard images and infrared target images in non-glass configuration were used to obtain the actual values. The results in Table I and Table II showed that Zhang's algorithm based on perspective camera model led to larger pose estimation error, while the proposed algorithm and Agrawal's were both effective, and the calibration results by proposed algorithm was closer to GT than Agrawal's. .

To verify the validity of the underground camera calibration algorithm, the proposed pose estimation system and the Vicon tracker were both used to obtain the trajectory of cutting-head synchronously. The platform is shown in Fig. 5d,e. Control the cutting-head to move in S-shaped motion path. Fig.10 and Fig.9 shows the comparison trajectory of the cutting-head with and without refraction compensation, respectively. It can be seen from Fig. 10 that the trajectory measured by the proposed method exhibits high consistent with the true trajectory. Fig. 11 shows the comparison trajectory of the cutting-head projected in the X-axis, Y-axis and Z-axis, respectively. The maximum position estimation error without refraction compensation was 56.61 mm, while the maximum position estimation error with refraction compensation by the proposed calibration method was decreased to 25.06 mm, which is close to the true value that obtained by the Vicon tracker. The results indicates that the pose estimation accuracy increases by 55.73%, The pose estimation meets the measurement accuracy requirement of Boom-type roadheader according to the underground tunneling safety rule that the maximum permissible error is within 50mm.

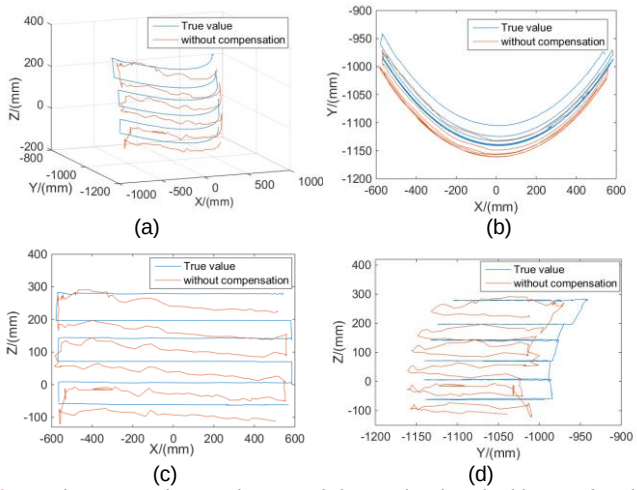

Fig.9. The comparison trajectory of the cutting-head without refraction compensation. (a) The comparison trajectory without refraction compensation. (b) The projection of the comparison trajectory on the XY plane. (c) The projection of the comparison trajectory on the XZ plane. (d) The projection of the comparison trajectory on the YZ plane.

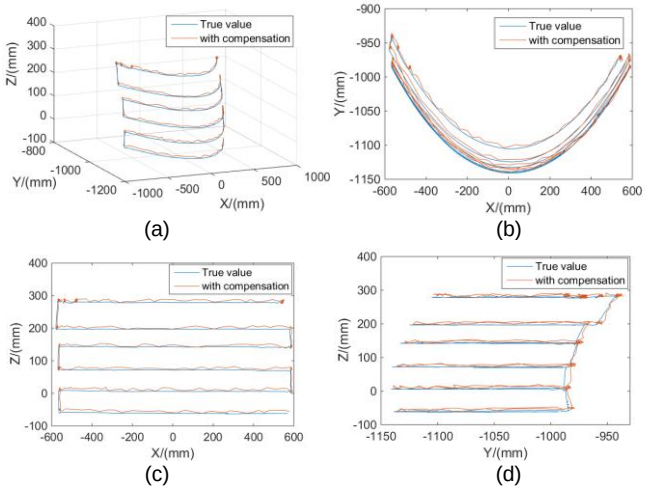

Fig.10. The comparison trajectory of the cutting-head with refraction compensation. (a)The comparison trajectory with refraction compensation. (b)The projection of the comparison trajectory on the XY plane. (c) The projection of the comparison trajectory on the XZ plane. (d) The projection of the comparison trajectory on the YZ plane.

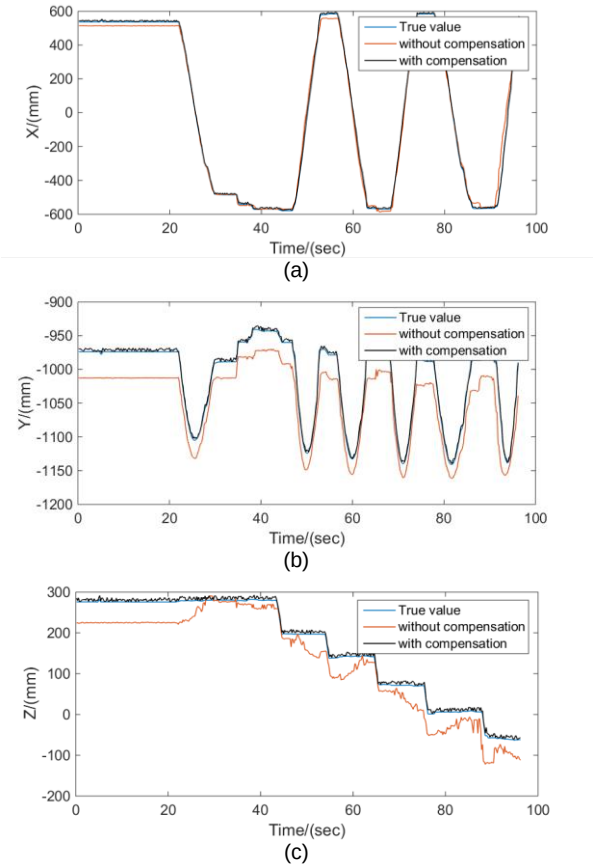

Fig.11. The comparison trajectory of the cutting-head. (a)The projection of the comparison trajectory in X-axis. (b)The projection of the comparison trajectory in Y-axis. (c)The projection of the comparison trajectory in Z-axis.

VI. Conclusion And Future Work

This paper proposed a geometrically-driven underground camera modeling and calibration method for Boom-type roadheader. An underground camera model was established under coplanarity constraints, which not only accounts for the refraction effect of the two-layer glasses but also preserve the collinearity relation. On this basis, the geometrically-driven calibration of underground camera was explored, the relative orientation between the camera and target was accurately described through refraction compensation. The hybrid LM-PSO algorithm was proposed to further optimize the calibration results. Experimental results confirmed that the image points distortion can be well rectified by the proposed calibration algorithm. Moreover, the infrared-LEDs target makes it affordable for underground camera calibration in coal mine. The accuracy of the geometrically-driven cutting-head pose estimation system was within 25.06 mm, which increased by 55.73% in comparison with the conventional methods. Future work will focus on the validation of the proposed method in real coal mining application.

References

[1] R. Wang, S. Wang, Y. Wang, M. Cai and M. Tan, "Vision-Based Autonomous Hovering for the Biomimetic Underwater Robot—RobCutt-II," in IEEE Transactions on Industrial Electronics, vol. 66, no. 11, pp. 8578-8588, Nov. 2019.

[2] Y. Zhang, P. Huang, K. Song and Z. Meng, "An Angles-Only Navigation and Control Scheme for Noncooperative Rendezvous Operations," in IEEE Transactions on Industrial Electronics, vol. 66, no. 11, pp. 8618-8627, Nov. 2019.

[3] Cai Luo, Leijian Yu, and Peng Ren. A Vision-Aided Approach to Perching a Bioinspired Unmanned Aerial Vehicle, IEEE Transactions on Industrial Electronics, PP(99):1-1,October 2017.

[4] A. Agrawal, S. Ramalingam, Y. Taguchi and V. Chari, "A theory of multi-layer flat refractive geometry," 2012 IEEE Conference on Computer Vision and Pattern Recognition, Providence, RI, 2012, pp. 3346-3353.

[5] R.Y. TSAI, An efficient and accurate camera calibration technique for 3D machine vision, in: Proc. ieee Conf. on Computer Vision & Pattern Recognition, 1986, pp.364–374.

[6] Z. Zhang, A flexible new technique for camera calibration, Pattern Anal. Mach. Intell. IEEE Trans. 22 (11) (2000) 1330–1334.

[7] Steger, C., Ulrich, M., and Wiedemann, C. (2008). Machine vision algorithms and applications. Weinheim: Wiley-VCH.

[8] R. I. Hartley and A. Zisserman. Multiple View Geometry in Computer Vision. Cambridge University Press, 2000.

[9] Z. Chen, K.-Y. K. Wong, Y. Matsushita, X. Zhu, and M. Liu. Self-calibrating depth from refraction. In ICCV, 2011.

[10] Bashar Elnashef, Sagi Filin. Direct linear and refraction-invariant pose estimation and calibration model for underwater imaging, ISPRS Journal of Photogrammetry and Remote Sensing, Volume 154, Pages 259-271, 2019.

[11] M. Alterman, Y. Y. Schechner, P. Perona, and J. Shamir. Detecting motion through dynamic refraction. IEEE TPAMI, 35(1):245–251, 2013.

[12] L. Kang, L. Wu, and Y.-H. Yang. Two-view underwater structure and motion for cameras under flat refractive interfaces. In Proc. of ECCV, pages 303–316, 2012.

[13] Shortis, M. R. and Harvey, E. S., 1998. Design and calibration of an underwater stereo-video system for the monitoring of marine fauna populations. International Archives Photogrammetry and Remote Sensing, 32(5): 792-799.

[14] Shortis, M.R., Seager, J.W., Williams, A., Barker, B.A., Sherlock, M., 2007b. A towed body stereo-video system for deep water benthic habitat surveys. In: Grün, A., Kahmen, H. (Eds.), Proc. Eighth Conference on Optical 3D Measurement Techniques, ETH Zurich, Switzerland, 2, pp. 150~157.

[15] Drap, P., Seinturier, J., Scaradozzi, D., Gambogi, P., Long, L., Gauch, F., 2007. Photogrammetry for virtual exploration of underwater archeological sites. In: Proc. XXIth CIPA International Symposium, Athens, Greece, 1–6 October.

[16] Y.H. Kwon and J.B. Casebolt, "Effects of Light Refraction on the Accuracy of Camera Calibration and Reconstruction in Underwater Motion Analysis," Sports Biomechanics, vol. 5, pp. 315-340,2006.

[17] T. Treibitz, Y. Y. Schechner, and H. Singh. Flat refractive geometry. In CVPR, 2008. 1, 2, 7

[18] Maas, H.G., New developments in multimedia photogrammetry. In: Grün, A.,Kahmen, H. (Eds.), Optical 3D Measurement Techniques III. 1995

[19] Y.-J. Chang and T. Chen. Multi-view 3D reconstruction for scenes under the refractive plane with known vertical direction. In ICCV, 2011.

[20] Wichmann Verlag, Karlsruhe. Gili Telem, Sagi Filin, Photogrammetric modeling of underwater environments, ISPRS Journal of Photogrammetry and Remote Sensing, Volume 65, Issue 5, September 2010, Pages 433-444

[21] Gili Telem, Sagi Filin, Photogrammetric modeling of the relative orientation in underwater environments, ISPRS Journal of Photogrammetry and Remote Sensing, Volume 86, December 2013, Pages 150-156

[22] A. Jordt-Sedlazeck and R. Koch. Refractive Structure-from-Motion on Underwater Images. In ICCV, pages 57-64, 2013

[23] Chen Xida, Yee-Hong Yang, Two-View Camera Housing Parameters Calibration for Multi-layer Flat Refractive Interface, Conference: 2014 IEEE Conference on Computer Vision and Pattern Recognition (CVPR), June 2014.

[24] J.-P. Tardif, P. Sturm, M. Trudeau, and S. Roy. Calibration of cameras with radially symmetric distortion. PAMI, 31(9):1552–1566, 2009. 1, 2.

[25] D. Nistér. An efficient solution to the five-point relative pose problem. PAMI, 26(6):756–770, June 2004. 1, 3

[26] Chen Lv, Yang Xing, Junzhi Zhang, Xiaoxiang Na, Yutong Li, Teng Liu, Dongpu Cao, Fei-Yue Wang, "Levenberg–Marquardt Backpropagation Training of Multilayer Neural Networks for State Estimation of a Safety-

Critical Cyber-Physical System," in IEEE Transactions on Industrial Informatics, vol. 14, no. 8, pp. 3436-3446, Aug. 2018.

[27] J. Shawash and D. R. Selviah, "Real-Time Nonlinear Parameter Estimation Using the Levenberg–Marquardt Algorithm on Field Programmable Gate Arrays," in IEEE Transactions on Industrial Electronics, vol. 60, no. 1, pp. 170-176, Jan. 2013.

[28] Li Deng, Gen Lu, Yuying Shao, Minrui Fei, Huosheng Hu, A novel camera calibration technique based on differential evolution particle swarm optimization algorithm, Neurocomputing, Vol 174, 2016,Pages 456-465

[29] Yukun Bao, Zhongyi Hu, Tao Xiong,A PSO and pattern search based memetic algorithm for SVMs parameters optimization, Neurocomputing, Volume 117,2013,Pages 98-106.